

Article

Fabrication of Poly(o/m-Toluidine)–SiC/Zinc Bilayer Coatings and Evaluation of Their Corrosion Resistances

Chuanbo Hu ^{1,2} , Ying Li ^{1,2,*}, Jiawei Zhang ^{1,2} and Wenlong Huang ^{1,2}

¹ School of Metallurgy, Northeastern University, Shenyang 110819, China; shifeng502@163.com (C.H.); zhang416940558@163.com (J.Z.); hwl3894368@gmail.com (W.H.)

² Liaoning Key Laboratory for Metallurgical Sensor and Technology, Northeastern University, Shenyang 110819, China

* Correspondence: liying@mail.neu.edu.cn

Received: 1 April 2018; Accepted: 5 May 2018; Published: 9 May 2018



Abstract: The purpose of this research was to study the structure and corrosion resistance of poly(o/m-toluidine)-SiC/zinc (Zn) bilayer coatings. Poly(o/m-toluidine) films, such as poly(o-toluidine) (POT) and poly(m-toluidine) (PMT), were chemically deposited on the surface of composite SiC/Zn coating using the solution evaporation method. The structures of poly(o/m-toluidine) were characterized by various optic techniques and the electrochemical behavior was studied by cyclic voltammetry (CV). The structures and morphologies of the SiC/Zn coating were detected by Fourier transformation infrared spectroscopy (FTIR), X-ray diffraction (XRD), energy dispersive spectrometer (EDS), and scanning electron microscopy (SEM). Thereafter, the corrosion resistances of electrodeposited and bilayer coatings were investigated in 3.5% NaCl solution by electrochemical corrosion techniques and an accelerated immersion test. The results showed that the outer POT film exhibits a lower corrosion behavior with respect to PMT, which significantly reduces the corrosion rate of SiC/Zn coating and prolongs the service life of the zinc matrix. The conclusion demonstrates that the stronger adsorptive POT film ensures the formed POT–SiC/Zn bilayer coatings possess a compact and low-defect surface, which facilitates POT film to develop its excellent barrier and passivation properties against corrosion.

Keywords: poly(o/m-toluidine); SiC/zinc; corrosion resistance; barrier; passivation

1. Introduction

Zinc (Zn) coatings are widely used on the surface of steel and iron, with the Zn coating acting as a sacrificial anode and cathodically protecting the underlying metal against corrosion [1]. However, an excellent coating must be defect free and compact enough to endure the attack of a corrosive environment [2]. Zn coatings contain some concave–convex structure, which seriously affects its corrosion protection [3]. The presence of different types of inorganic nanoparticles in the zinc matrix has been reported to increase the coating compactness and consequently improve the corrosion behavior of the Zn coating [4–6]. Praveen et al. [7] found that the incorporation of TiO₂ nanoparticles in the zinc matrix led to improvement in the crystal size and enhanced the corrosion resistance, microhardness, and wear resistance properties of the composite coating. Although Zn and its composite coatings have excellent surface and corrosion characteristics, Zn substrate in humid environments is easily susceptible to the formation of white-rust corrosion products which significantly reduce the zinc-matrix lifetime. In general, white rust is prevented by subjecting the Zn coating to post-plating process, such as chrome passivation, or generating a thin film which provides a barrier layer between the Zn coating and the corrosion environment [8,9]. Although the formation of white rust can be avoided by chromating Zn

substrate, the chromium in chromates is a heavy metal which could bring serious hazards to humans and the environment. Therefore, looking for an effective method that can substitute chromating has become essential in the electrodeposition zinc industry.

In the past few decades, conducting polymers have been widely used for corrosion protection due to their unique conduction mechanisms [10]. Compared to paints and cadmium containing coatings, the advantage of conducting polymer films is that they do not contain toxic substances that are harmful to the environment and they act both as a physical and electronic barrier [11], improving the protection afforded by paints that simply act as a physical barrier alone. The electronic barrier is considered to be based on the conduction mechanism of conducting polymers to form passivation oxide layers at the interface of metal and the coating film to improve the total barrier capability of the coating. The most studied conducting polymers are polypyrrole (PPy) and polyaniline (PANI), which are applied on the surface of oxidizable metals or alloys [12]. Lehr et al. [13] and Sheng et al. [14] found that Zn-PPy bilayer system is a very effective protective coating for steel and magnesium alloy. Tüken et al. [15] suggested that the inner Zn acts as a sacrificial anode against the corrosion of mild steel and the outer PANI behaves as a physical barrier to prevent the permeation of corrosion medium. Therefore, the assembly of conducting polymer films onto the galvanized steel surfaces to fabricate the bilayer coatings is a promising approach for protection of Zn or its composite electrodeposited coatings against corrosion.

It is well known that the ring substituted modification of PANI usually can improve the solubility, conductivity, thermal stability, and corrosion resistance of PANI derivatives [16]. Bilal et al. [17] and our group [18] have confirmed the excellent structure and corrosion resistance of poly(o-toluidine). As a very stable inorganic material, silicon carbide (SiC) has been widely used in the reinforcement phase of composite materials or coatings [19]. Based on that, in order to study the effect of methyl substituent on the structure and corrosion resistance of PANI, we synthesized poly(o/m-toluidine) and applied it to the surface of composite SiC/Zn coating. In our recent investigations [20], we found that the corrosion protection effect of poly(o-ethylaniline) on composite SiC/Zn coating is stronger than that of poly(o-ethylaniline)/SiC composite to pure Zn coating, which indicates that the corrosion resistance of bilayer coating is dependent on the interaction between the inner/outer coating films. Therefore, in order to avoid the anodic oxidation defects of galvanized steel and expand the industrial applications of bilayer coatings, the fabrication procedure of bilayer coatings mainly takes three steps. Firstly, poly(o-toluidine) (POT) and poly(m-toluidine) (PMT) were synthesized by chemical oxidative polymerization method. Secondly, SiC/Zn coating was deposited on the carbon steel substrate by electrodeposition technique. Finally, the poly(o/m-toluidine) was applied on the surfaces of composite SiC/Zn coating to obtain POT-SiC/Zn and PMT-SiC/Zn bilayer coatings, respectively. The structures of poly(o/m-toluidine) and electrodeposited coatings were analyzed. The corrosion resistances of the electrodeposited and bilayer coatings were evaluated in 3.5% NaCl solution by electrochemical corrosion techniques and an accelerated immersion test.

2. Experimental

2.1. Materials

O-toluidine (OT) and M-toluidine (MT) monomers were obtained from Shanghai Macklin Biochemical Co., Ltd., (Shanghai, China) and they were distilled to colorless before use. Dodecylbenzene sulfonic acid (DBSA) was acquired from Linyi Yongtai Chemical Co., Ltd., (Linyi, China). Ammonium persulfate (APS) and zinc sulfate heptahydrate ($\text{ZnSO}_4 \cdot 7\text{H}_2\text{O}$) were purchased from Tianjin Kemiou Chemical Reagent Co., Ltd., (Tianjin, China). Sodium dodecyl benzene sulfonate (SDBS) was provided by Sinopharm Chemical Reagent Co., Ltd., (Shanghai, China). The SiC with an average size of 40 nm, supplied by Shanghai Chaowei Nanotechnology Co., Ltd., (Shanghai, China). Nmethyl-2-pyrrolidone (NMP) was provided by Tianjin Guangfu Fine Chemical Research Institute (Tianjin, China). The other reagents were purchased from different resources and used without further purification.

2.2. Synthesis of Poly(o/m-Toluidine)

Poly(o/m-toluidine), which includes poly(o-toluidine) (POT) and poly(m-toluidine) (PMT), was synthesized by chemical oxidative polymerization method. A given amount of DBSA and monomers were mixed according to the molar ratio of 1:1. The typical synthesis process of poly(o/m-toluidine) is as follows: 9.79 g of DBSA was dissolved in deionized water and added into 3.19 mL of OT monomer (or 3.25 mL of MT monomer) to form a mixture emulsion under a series of ultrasonic vibrating, magnetic, and vigorous stirrings, and then 100 mL of 0.3 M APS solution was added dropwise into the above mixture. The resulting mixture was allowed to react for 10 h below 5 °C. After that, the precipitate was collected on a Buchner funnel and washed multiple times with ethanol and deionized water. Finally, the products were dried in an oven at 60 °C for 24 h and then fine grinded by agate mortar.

2.3. Fabrication of Poly(o/m-Toluidine)-SiC/Zn Coatings

2.3.1. Electrodeposition of SiC/Zn Surface

According to our more recent study [20], the SiC/Zn coating can be electrodeposited on the surface of a carbon steel coupon (2 cm × 2 cm). Before the electrodeposition, the carbon steel coupon underwent a series of processes such as polishing, degreasing, pickling, rinsing, and drying. The optimized electrolyte contained 220 g/L of ZnSO₄·7H₂O, 3.2 g/L of SiC nanoparticles and 0.6 g/L of SDBS surfactant, which was magnetically stirred for 6 h at 25 °C and the pH was adjusted to 2.0 by 50 g/L of H₂SO₄ solution. The electrodeposition process was carried out in a two-electrode system: a piece of Ti-IrO₂ coupon was used as the anode and the steel coupon was used as the cathode in a standard electrolyte cell, respectively. In the electrodeposition process, a direct current (DC) power with 0.17 A/cm² current densities was applied to two electrodes at 40 °C for 15 min. After that, the electrodeposited SiC/Zn surface was rinsed with deionized water and airdried. Using the same method, the pure Zn surface on the steel substrate was also electrodeposited without SiC nanoparticles and SDBS surfactant in order to compare the structure and corrosion resistance. The thickness of the Zn and SiC/Zn coating films were measured by AIRAJ micrometer, which was about 130 μm.

2.3.2. Chemical Deposition of Poly(o/m-Toluidine) Films

The bilayer coatings were fabricated by solution evaporation method. Firstly, 0.5 g of POT or PMT was dissolved in 30 mL of NMP solution under ultrasonic vibrating for 30 min and magnetic stirring for 24 h at room temperature. Secondly, drops of the poly(o/m-toluidine)-NMP solution were spread on SiC/Zn surfaces. Finally, the casted polymer films were dried under vacuum at 50 °C for 12 h to evaporate the solvent. After the solvent evaporated completely, the poly(o/m-toluidine)-SiC/Zn bilayer coatings were thus obtained, and the thickness test shows that the thickness of the outer coating films was between 20 and 50 μm. Figure 1 shows the schematic diagram fabrication of poly(o/m-toluidine)-SiC/Zn bilayer coatings onto the carbon steel substrate.

2.4. Characterization

The FTIR spectra of samples were characterized using a Fourier transformation infrared spectrometer (Nicolet 380, Waltham, MA, USA) in the range of 500–4000 cm⁻¹. The XRD patterns of samples were conducted using a X-ray diffractometer (UltimaIV, Tokyo, Japan) in the range of 10°–90°. The chemical composition and structure of poly(o/m-toluidine) were performed using a X-ray photoelectron spectrometer (Escalab 250Xi, Waltham, MA, USA). The morphologies of poly(o/m-toluidine) were obtained using a field emission scanning electron microscope (FESEM, SU8010, Tokyo, Japan) and transmission electron microscope (TEM, JEM-2100, Tokyo, Japan). The electrochemical behavior of poly(o/m-toluidine) was performed using a cyclic voltammetry technique. A saturated calomel electrode (SCE) was the reference electrode, a platinum plate was the counter electrode, and a piece of carbon paper loaded with poly(o/m-toluidine) films was the working electrode. CV tests were carried out on the electrochemical workstation (VersaSTAT3, San Diego, CA,

USA) within a potential window between -0.2 to 1.0 V at scan rate of 20 mV/s, with the electrolyte being a 1.0 M HCl solution.

The surface morphologies and chemical compositions of the coatings were obtained using a scanning electron microscope (SEM, Ultra Plus, Heidenheim, Germany) equipped with an energy dispersive spectrometer (EDS, Ultra Plus). The electrochemical corrosion behaviors of the coatings were studied by Tafel polarization curves and electrochemical impedance spectroscopy (EIS) in a typical three-electrode system: an SCE as the reference electrode, a platinum plate as the counter electrode, and the coatings with an exposed area of 1.0 cm² as the working electrode. The electrochemical measurements were run on a VersaSTAT3 electrochemical workstation in 3.5% NaCl solution at room temperature. Tafel polarization curves were measured by automatically changing the potential from -250 to 250 mV versus the open circuit potential with a constant scan rate of 1 mV/s. EIS were performed at the open circuit potential with a frequency range of 100 kHz to 10 MHz with an amplitude of 10 mV, and the EIS data were analyzed by the fitting software (Zview2.0, Southern Pines, NC, USA). Furthermore, the electrodeposited and bilayer coatings were immersed in 3.5% NaCl solution for 90 days to accelerate the corrosion of the coated steels, and then the corrosion morphologies of coating surfaces were observed using a field emission scanning electron microscope (FEG250, Hillsboro, OR, USA).

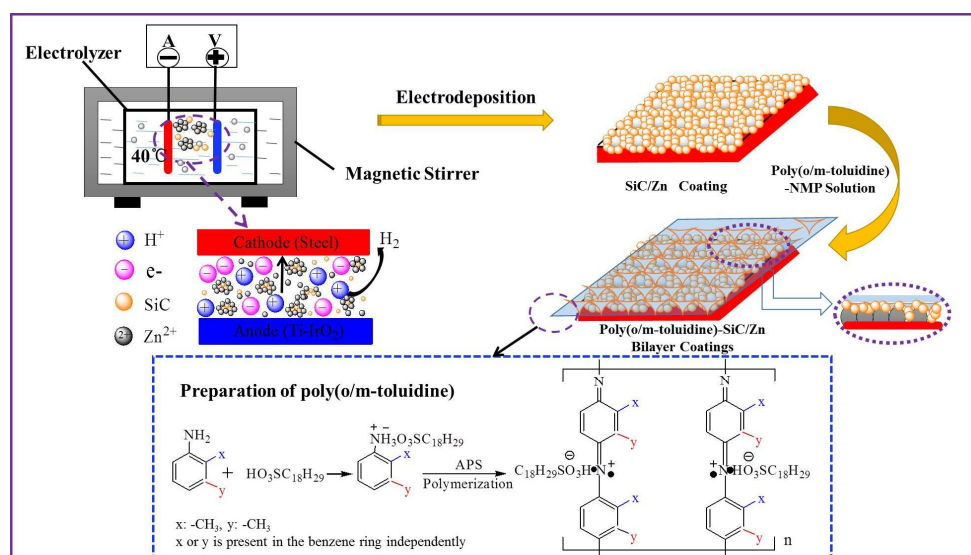


Figure 1. The schematic diagram fabrication of poly(o/m-toluidine)-SiC/Zn bilayer coatings.

3. Results and Discussion

3.1. Structural Analysis of Poly(o/m-Toluidine) Powders

The FTIR spectra and XRD patterns of poly(o/m-toluidine) are shown in Figure 2. As shown in Figure 2a, the main characteristic peaks of POT are consistent with the literatures [21,22]. The peak at 3452 cm⁻¹ is attributed to N–H stretching, which suggests the presence of –NH– groups in OT units. The peak at 2922 cm⁻¹ is caused by C–H stretching of the substituent methyl group. The peaks at 1608 and 1492 cm⁻¹ are characteristic of quinoid (Q) and benzenoid (B) rings, and the presence of Q and B clearly shows that POT is composed of the amine and imine units. The peak at 1326 cm⁻¹ is attributed to C–N stretching linked to benzene rings. The peaks at 1170 and 1017 cm⁻¹ are ascribed to the 1–4 substitution on the phenyl ring. The peaks at 1116 and 818 cm⁻¹ reveal C–H bending of quinoid and benzenoid rings. Furthermore, the peak at 2922 cm⁻¹ is also ascribed to C–H stretching in the methyl group of DBSA [23], with the result indicating that DBSA has been doped in POT chains. The FTIR spectra of PMT shows the main characteristic peaks have insignificantly changed. These results confirm that the position of the methyl group has no effect on the characteristic absorption peak of PMT.

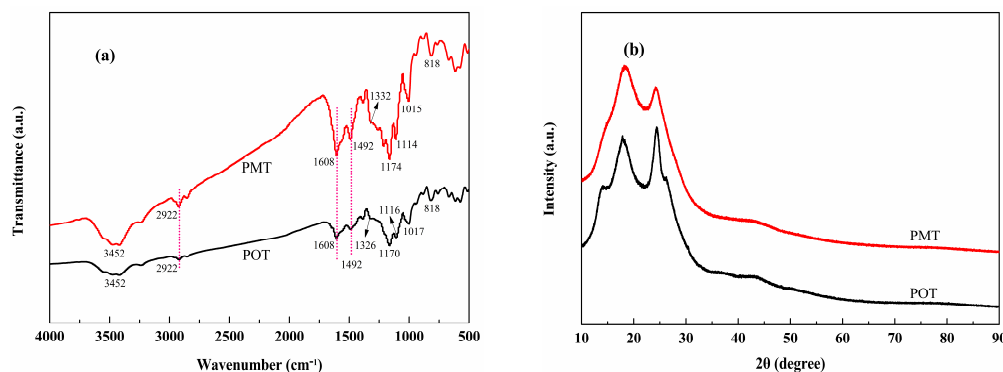


Figure 2. Structure analysis of poly(o-toluidine) (POT) and poly(m-toluidine) (PMT): (a) Fourier transformation infrared spectroscopy (FTIR) spectra and (b) X-ray diffraction (XRD) patterns.

The XRD patterns of poly(o/m-toluidine) are illustrated in Figure 2b. As shown in Figure 2b, both polymers display two pointed diffraction peaks between 17° and 25° . It should be noted that the amorphous scattering of PANI appears at around 18° , and the characteristic diffraction peak at approximately 25° is related to the interplanar distance of aniline-aniline [24]. After doping POT with DBSA, the broad halo arising from amorphous polymer decreases while the intensity of the diffraction peak at 2θ about 25° visibly grows, indicating that the amorphous polymer is decreasing, with the more ordered structure of crystalline polymer appearing. According to previous studies [25], DBSA dopant evidently increases the crystalline behavior of POT due to the protonation of intercalated DBSA between the polymer chains. On the contrary, PMT shows that the intensity of the crystalline polymer structure is weaker than that of amorphous polymer. The results indicate that the ortho-methyl would extend the molecular chains of PANIs and improve the regularity between the chains, which promotes the semi-crystalline nature of polymers and thus improves the diffraction intensity of POT.

The survey X-ray photoelectron spectroscopy (XPS) spectra and the fitted N 1s peaks of poly(o/m-toluidine) are shown in Figure 3. As shown in Figure 3a, the wide range XPS spectra of POT and PMT show clearly visible C 1s, N 1s, O 1s, and S 2p peaks, and their binding energies are mainly located at around 284.24, 398.97, 531.35, and 167.93 eV, respectively. The O 1s and S 2p peaks are derived from APS byproducts and DBSA dopants, which demonstrates that the both polymers have formed and are present as the doped state. Figure 3b shows the N 1s peaks of POT could be fitted into imine ($=N-$), amine ($-NH-$), protonated amine ($-NH_2^+$), and protonated imine ($=NH^+$). Figure 3c shows the same fitting peaks exist in the N 1s peak of PMT and the position changes of binding energies are very little. Golczak et al. [26] think that the conductivity of polymers is proportional to the doping level, and a higher doping level is related to higher conductivity. PANI or its derivatives can achieve a high conductive state through the protonation of the imine nitrogens in its emeraldine state. Since the doped acids adsorb preferentially on the imine nitrogens, the protonation degree can be estimated from the area ratio of cationic nitrogen and the sum of cationic nitrogen and imine nitrogen [26,27]. The protonation degrees of POT and PMT are estimated to be approximately 48.51% and 45.54%. The results indicate that the ortho-methyl in POT exerts a positive mesomeric effect which increases the electron density at the nitrogen atom [28], and that POT achieves higher protonation and obtains more doping.

The surface morphologies of POT and PMT were characterized by FESEM and TEM. As shown in Figure 4a,b, the FESEM images of POT and PMT all show the aggregated structures. The PMT display a larger lumpy structure with the diameter range of 10–15 μm . In the case of POT, a relatively uniform and small flaky shaped structure was formed with an average outer diameter of 2.5 μm . TEM images of POT and PMT are shown in Figure 4c,d. It can be found that the morphology of PMT is dominated by irregularly shaped, highly disordered agglomerates, while the morphology of POT shows smaller irregular tight agglomerates, and POT seems to be more compact than PMT. The surface

morphologies of POT and PMT reveal that the positions of the methyl have a strong effect on the structure of poly(o/m-toluidine).

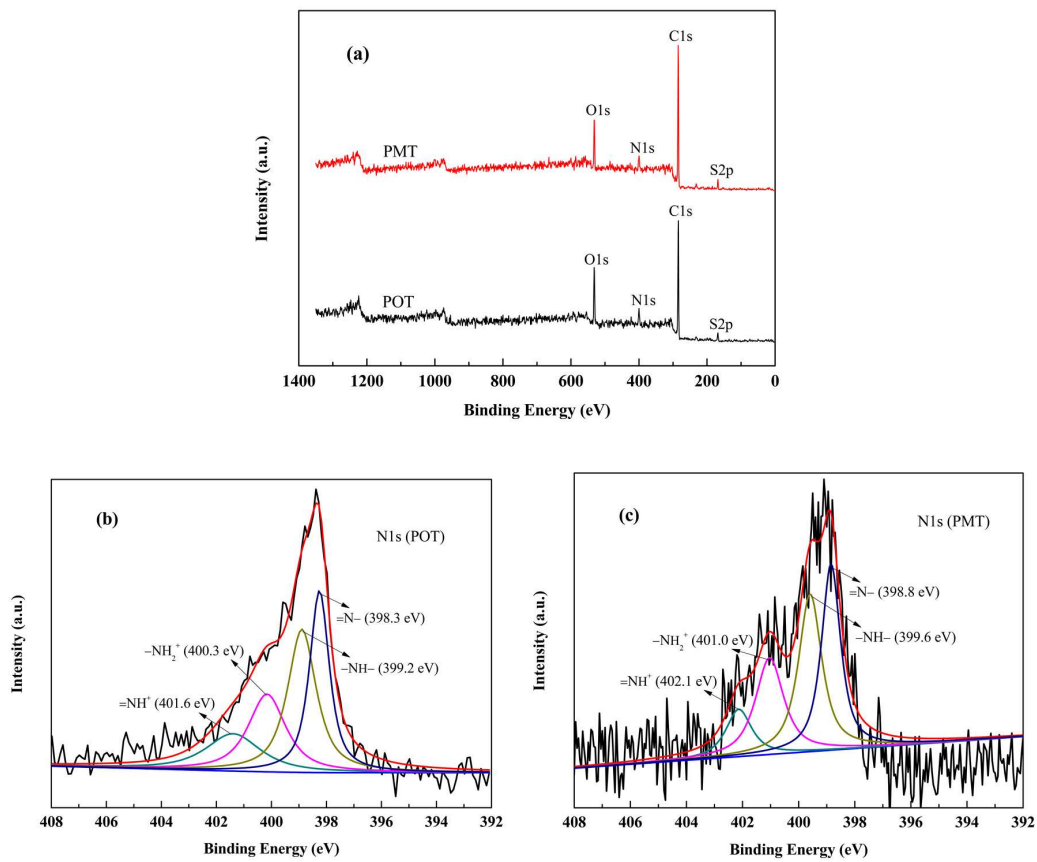


Figure 3. X-ray photoelectron spectroscopy (XPS) spectra of (a) survey; N 1s peaks of (b) POT and (c) PMT.

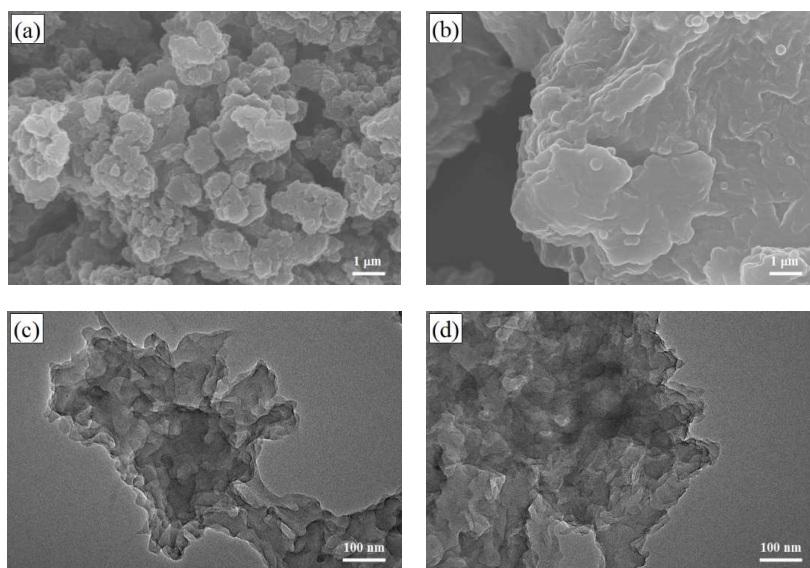


Figure 4. Field emission scanning electron microscopy (FESEM) images of (a) POT and (b) PMT; Transmission electron microscopy (TEM) images of (c) POT and (d) PMT.

3.2. Electrochemical Behavior of Poly(o/m-Toluidine) Films

Cyclic voltammetry (CV) has been widely performed to evaluate the electrochemical activity and stability of conducting polymers. The CV curves of POT and PMT films scanning 1 and 10 cycles in 1.0 M HCl solution are shown in Figure 5. As shown in Figure 5a, the shape of both curves is almost the same and they display a typical two couples of redox peaks of PANI [29]. In general, the redox peaks in the CV curves of PANI were ascribed to the conversions between leucoemeraldine/emeraldine and emeraldine/parnigraniline [30]. The CV curves of poly(o/m-toluidine) show the same pseudocapacitance behavior of the conducting polymer as that of PANI. The well-defined oxidation/reduction peaks confirm the good electrochemical activity of both polymers, and indicate that POT and PMT are reversible. Herein, it is found that the peak area of POT is larger than that of PMT at the same scan rate, suggesting the electrochemical activity of POT is higher than PMT. The increased electrochemical activity of POT can be explained by the higher electron-donating effects. The ortho-position methyl can lead to an increase of the electronic density states, which facilitates the protonation of the amine group and the formation of the polaron/bipolaron states [31]. In addition, the higher protonation of POT would also result in an increase in the electrical conductivity and the peak current, and thus promote the redox reaction of polymers chains. Generally, conducting polymers would undergo electrochemical degradation during the redox process. Therefore, the stability of polymer films has been studied by applying continuous potential scans in monomer-free electrolyte solution and after that comparing the CV curves of the initial and final potential scans [32]. As illustrated in Figure 5b, it was found that the shapes of CV curves for both polymers have almost no change after 10 cycles of scanning, which indicates that POT and PMT have excellent electrochemical stability.

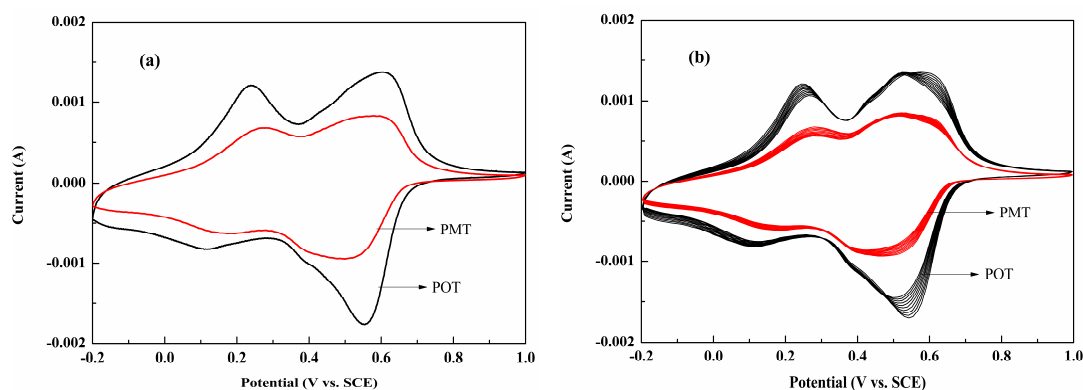


Figure 5. CV curves of POT and PMT films immersed in 1.0 M HCl solution: (a) 1 cycle and (b) consecutively scanning 10 cycles at 20 mV/s scan rate.

3.3. Structural Analysis of Electrodeposited Coatings

The structure and chemical compositions of the electrodeposited coatings were investigated by FTIR, XRD, and EDS. Figure 6a shows that a weak peak at 812 cm^{-1} in the FTIR spectra of SiC/Zn coating was detected. This peak is in accordance with the characteristic absorption peak of SiC nanoparticles located at 816 cm^{-1} . The decrease of the absorption intensity indicates that SiC nanoparticles have been dispersed on the inside of the Zn matrix and have formed a composite surface. Figure 6b shows the XRD patterns of both electrodeposited coatings. The six main characteristic diffraction peaks of Zn coating are found at 2θ about 36.2° , 38.8° , 43.2° , 54.3° , 70.2° , and 82.1° , which corresponds to the crystal planes of Zn (002), Zn (100), Zn (101), Zn (102), Zn (110), and Zn (112) [2,33]. The diffraction pattern of the SiC/Zn coating contains the phases of pure zinc and SiC, and the partial diffraction peaks of SiC have overlapped with Zn due to the coverage effects, indicating that the SiC/Zn coating has been successfully electrodeposited on the surface of the steel coupon. Figure 6c

shows the EDS spectra of Zn and SiC/Zn coatings. It can be seen from Figure 6c that the Zn coating mainly contains Zn element, while the SiC/Zn coating consists of C, Si, and Zn elements, further supporting the conclusions that the SiC/Zn coating has been successfully electrodeposited on the steel substrate.

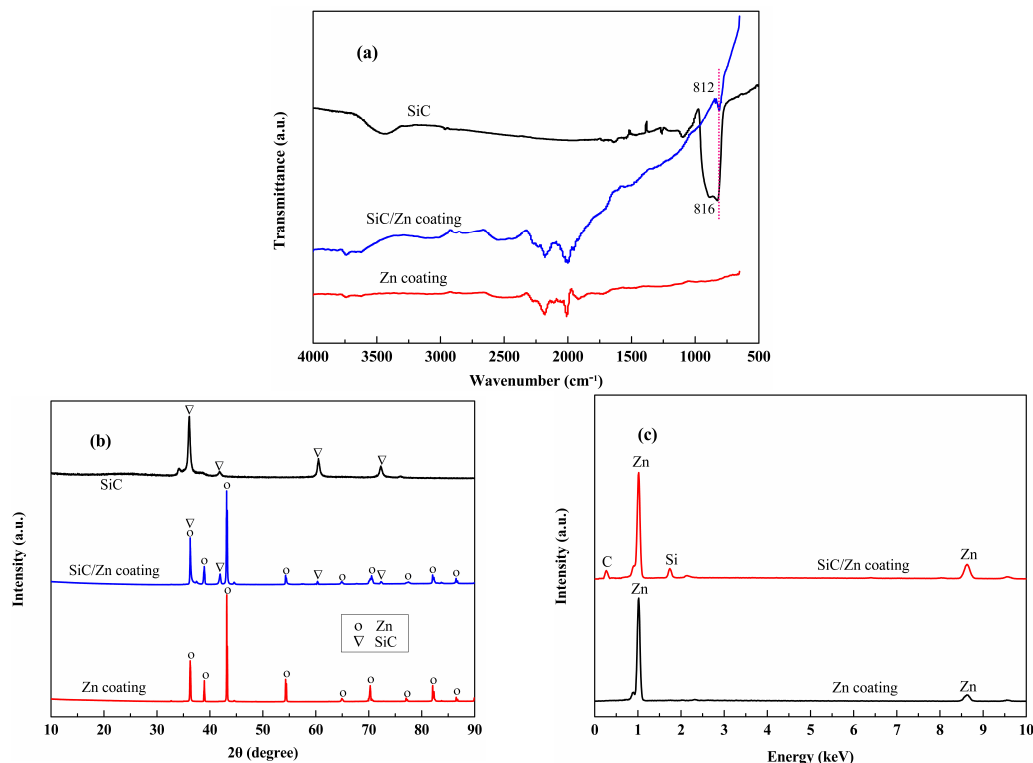


Figure 6. Structure analysis of Zn and SiC/Zn coatings: (a) FTIR spectra; (b) XRD patterns and (c) Energy dispersive spectrometer (EDS) spectra.

3.4. Surface Characterization of Electrodeposited and Bilayer Coatings

The surface morphologies of the coatings are depicted in Figure 7. From Figure 7a and the inset, it can be seen that the surface of the pure Zn coating shows some sheet-like bulges. These structures that present a rough appearance can easily cause grooves and pores defects. As can be seen from Figure 7b and its inset, some SiC nanoparticles were incorporated on the pores of the Zn coating and that some additional particles were randomly adsorbed on the coating surface, which lead to the composite SiC/Zn coating to show a compact surface with micro/nanostructure. The increase in compactness of SiC/Zn coating may be due to SiC nanoparticles possessing a negative surface charge at pH = 2 and the Zn²⁺ ions surrounding the nanoparticles giving them an overall positive surface charge, resulting in co-deposition at the negatively charged cathode [34]. Moreover, the co-deposition was also a competition process between Zn²⁺ ions and SiC nanoparticles for the surface active sites. The incorporation or adsorption of these nanoparticles at the active growth sites of the crystal would restrain its growth, and consequently, a finer grained structure would be obtained [35]. Figure 7c depicts that the surface of POT-SiC/Zn coating was rough and crack-free, although Figure 7d reveals that PMT-SiC/Zn coating is relatively rough and porous. The rough structures were gradually decreased once poly(o/m-toluidine) was applied on the surface of the SiC/Zn coatings, with the POT-SiC/Zn coating being more compact and low-defect. From the study of Benchikh et al. [36], we deduce that the ortho-PANI derivatives can produce a stable Zn–N co-ordination bond between the POT film and the SiC/Zn surface due to the higher π -electron effect of the ortho-methyl group, and can improve the adsorption strength of the POT film to the SiC/Zn surface. In addition, the

micro/nanostructure of the SiC/Zn surface is also beneficial in producing good inlay bonding between the POT film and the SiC/Zn surface, thus eliminating the existence of residual air and forming compact and crack-free bilayer coatings.

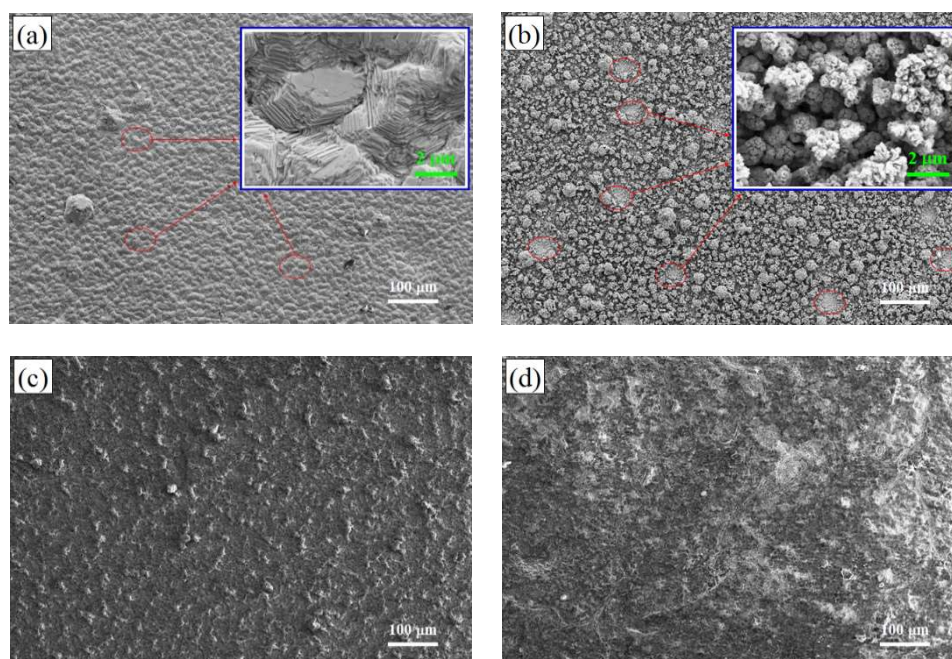


Figure 7. Scanning electron microscopy (SEM) images of (a) Zn; (b) SiC/Zn; (c) POT-SiC/Zn and (d) PMT-SiC/Zn coatings.

3.5. Corrosion Resistances of Electrodeposited and Bilayer Coatings

The Tafel plots of the electrodeposited and bilayer coatings after immersion in 3.5% NaCl solution for 168 h are depicted in Figure 8, and the corrosion characteristics of all coatings calculated by the Tafel extrapolation method are listed in Table 1. It can be seen from Figure 8 that the Zn coating has a lower corrosion potential (E_{corr}) and higher corrosion current density (I_{corr}), which corresponds to the immersion of the Zn surface in 3.5% NaCl solution, causing the groove structures of the Zn coating to form an air-formed layer [37], with the cathodic reaction easily occurring inside of the grooves. The addition of SiC nanoparticles moved the Tafel plot of the SiC/Zn coating in the positive direction, and the improvement in corrosion resistance of the zinc matrix mainly arises from three effects of SiC nanoparticles [38,39]. First, the co-deposition of the SiC/Zn coating holds a compact surface with micro/nanostructure. In these structures, Zn acts as an anode and SiC acts as a cathode, which facilitates anodic polarization and consequently only homogenous corrosion occurs. Second, SiC nanoparticles fill the grooves and pores of the Zn matrix, reducing the coating defect. The uniformly distributed nanoparticles serve as physical barriers to block the penetration of the corrosive medium. Third, incorporation of SiC nanoparticles decreases the available metallic area for corrosion.

As shown in Table 1, a positive shift in E_{corr} values of 208 and 126 mV and a decrease in the I_{corr} values of 3- and 2-fold have been found when POT and PMT were applied to the surface of the SiC/Zn coating. The positive shift in the E_{corr} and substantial reduction in the I_{corr} of the SiC/Zn coating reveals the anticorrosion character of conducting polymers, which indicates that the outer polymer films have provided effective protection for the SiC/Zn surfaces. The protection efficiency (PE) of composite and bilayer coatings was calculated by the following equation [40]:

$$PE(\%) = \frac{I_{corr} - I'_{corr}}{I_{corr}} \times 100$$

where I_{corr} and is the corrosion current density of the Zn coating and I'_{corr} is the corrosion current density of composite and bilayer coatings. Compared to the electrodeposited coatings, the protection efficiencies of bilayer coatings have been improved significantly. These results indicate that the assembled outer polymer films can effectively protect the SiC/Zn surface and that the POT film is more protective. The improved corrosion protection ability of the composite coating is derived from the physical and electronic barrier effects of conducting polymers [12,16]. The poly(o/m-toluidine) was similar to PANI, exhibiting a redox potential close to silver, which could ennoble the available zinc surfaces and form one or more layers of passive oxide films on the surface of the SiC/Zn coating. In general, the efficiency of an organic coating as a successful corrosion inhibitor mainly depends on its capability to get adsorbed on the metallic surface [41]. As described in Figure 7, the stronger adsorptive and continuous POT film would form a denser passivation film on the surface of the SiC/Zn coating during the corrosion reaction, thus facilitating the POT-SiC/Zn coating to exhibit multiple barrier effects to against corrosion.

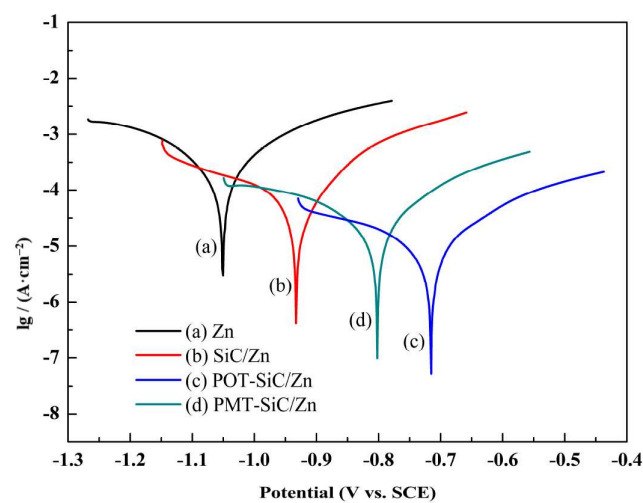


Figure 8. Tafel plots of electrodeposited and bilayer coatings after immersed in 3.5% NaCl solution 168 h.

Table 1. Fitting corrosion parameters for electrodeposited and bilayer coatings after immersed in 3.5% NaCl solution for 168 h by Tafel polarization and electrochemical impedance spectroscopy (EIS) methods.

Coatings	Tafel Method				Impedance Method				
	E_{corr} (V)	I_{corr} (A/cm ²)	PE (%)	R_s (Ω·cm ²)	CPE_c (F/cm ²)	R_p (Ω·cm ²)	CPE_{dl} (F/cm ²)	R_{ct} (Ω·cm ²)	PE (%)
Zn	−1.05	9.77×10^{-4}	–	7.67	1.83×10^{-5}	67.51	3.38×10^{-4}	1938	–
SiC/Zn	−0.931	2.29×10^{-5}	76.56	13.03	5.65×10^{-6}	112.63	1.83×10^{-4}	4517	57.09
POT-SiC/Zn	−0.723	8.71×10^{-6}	91.08	30.92	8.57×10^{-7}	233.70	5.94×10^{-5}	8903	78.23
PMT-SiC/Zn	−0.805	1.17×10^{-5}	88.02	21.28	1.21×10^{-6}	187.90	8.53×10^{-5}	6609	70.68

Figure 9 shows the Nyquist complex plane plots of electrodeposited and bilayer coatings after immersion in 3.5% NaCl solution for 168 h. These plots were analyzed using the same equivalent circuit shown in the illustration of Figure 9, where R_s represents the electrolyte solution resistance, CPE_c is the constant phase element implying the coating capacitance, R_p represents the coating pore resistance, CPE_{dl} is the constant phase element indicating the double layer capacitance, and R_{ct} represents the charge transfer resistance. From Figure 9, it can be found that the electrodeposited coatings display a depressed semicircle and the Nyquist plots can be fitted into two semicircles. The smaller semicircle characterizes the formation of corrosion film on the surface of the zinc matrix, and the larger semicircle means the corrosion processes occur underneath the corrosion film [42]. The mechanism of metal or its alloy coatings has been confirmed by Chaudhari et al. [42,43]. The fitting impedance parameters

by the equivalent circuit are given in Table 1, with all the values of exponent n in the $CPEs$ elements recorded at 0.8–1.0. As shown in Table 1, the incorporation of SiC nanoparticles has improved the corrosion resistance of the Zn matrix. The increases of R_{ct} and the decreases of CPE_{dl} in the case of SiC/Zn coating can be attributed to the existence of a compact surface with micro/nanostructure, which leads to a decrease of the active area directly in contact with the corrosion medium.

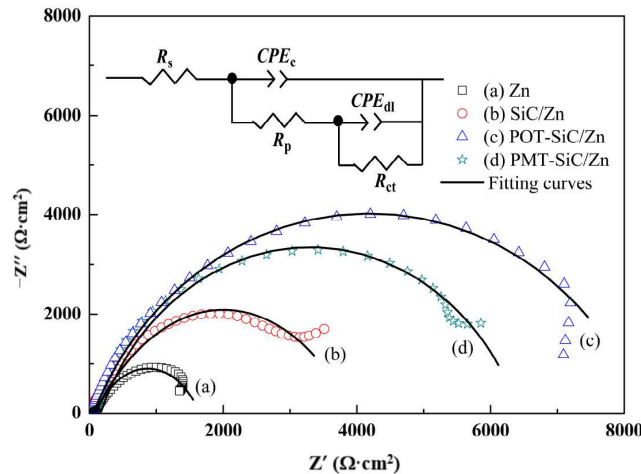


Figure 9. Nyquist plots of electrodeposited and bilayer coatings after immersion in 3.5% NaCl solution for 168 h.

As shown in Figure 9c,d, the Nyquist plots of bilayer coatings display the same semicircle characteristic as that of electrodeposited coatings. The first semicircle expresses the interface of polymer films/electrolyte and it is characterized by the CPE_c and R_p . The second semicircle expresses the interface of polymer films/zinc matrix and it is characterized by the CPE_{dl} and R_{ct} . The R_p values of POT-SiC/Zn and PMT-SiC/Zn coatings are 3.5- and 2.8-fold higher than the Zn coating and 2- and 1.7-fold higher than the SiC/Zn coating, which indicates that the porosity in the poly(o/m-toluidine)-SiC/Zn coatings are considerably lower than that of Zn and SiC/Zn coatings. In addition, the R_{ct} values of POT-SiC/Zn and PMT-SiC/Zn coatings are found to be about 4.6- and 3.4-fold higher than the Zn coating and 2- and 1.5-fold higher than the SiC/Zn coating. The higher R_{ct} is attributed to the effective barrier behavior of the outer polymer films [44], and the barrier effect of POT film is stronger. The better performance of POT film than that of PMT film may be due to its relatively good adsorption strength and the formed continuous outer film, so it can form a denser and more uniform passivation film on the surface of the SiC/Zn coating during the corrosion reaction, and thus increase the total barrier effect of bilayer coatings. Generally, a uniform, defect-free coating with corrosion resistance is characterized by higher R_p and R_{ct} and lower CPE_c and CPE_{dl} [45]. The lower CPE_c and CPE_{dl} of POT-SiC/Zn bilayer coatings further prove the protection of the SiC/Zn surface by POT. Therefore, all results indicate the outer POT film would provide excellent protection to the inner SiC/Zn surface. According to the fitted R_{ct} values, the protection efficiency (PE) of composite and bilayer coatings was also calculated by the expression [40]:

$$PE(\%) = \frac{R_{ct} - R'_{ct}}{R_{ct}} \times 100\%$$

where R'_{ct} denotes the charge transfer resistance of the Zn coating and R_{ct} denotes the charge transfer resistance of composite and bilayer coatings. The protection efficiency calculated from the above expression is shown in Table 1, it can be seen that the protection efficiencies of bilayer coatings are always higher than that of monolayer coatings, and POT-SiC/Zn coating is more protective. This result is consistent with the Tafel polarization tests.

The corrosion morphologies of electrodeposited and bilayer coatings were also observed after being immersed in 3.5% NaCl solution for 90 days. As shown in Figure 10a, many deep corrosion pits and large corrosion products exist on the surface of the Zn coating. Figure 10b shows that some small corrosion pits and corrosion products are distributed on the surface of the SiC/Zn coating, meaning that SiC nanoparticles fill pores and groove defects of the Zn coating, which decreases the metallic area available for corrosion significantly. From Figure 10c,d, it can be seen that no severe corrosion was distributed on the surfaces of the poly(o/m-toluidine)-SiC/Zn coating, and that the POT film is denser and less porous than the PMT film.

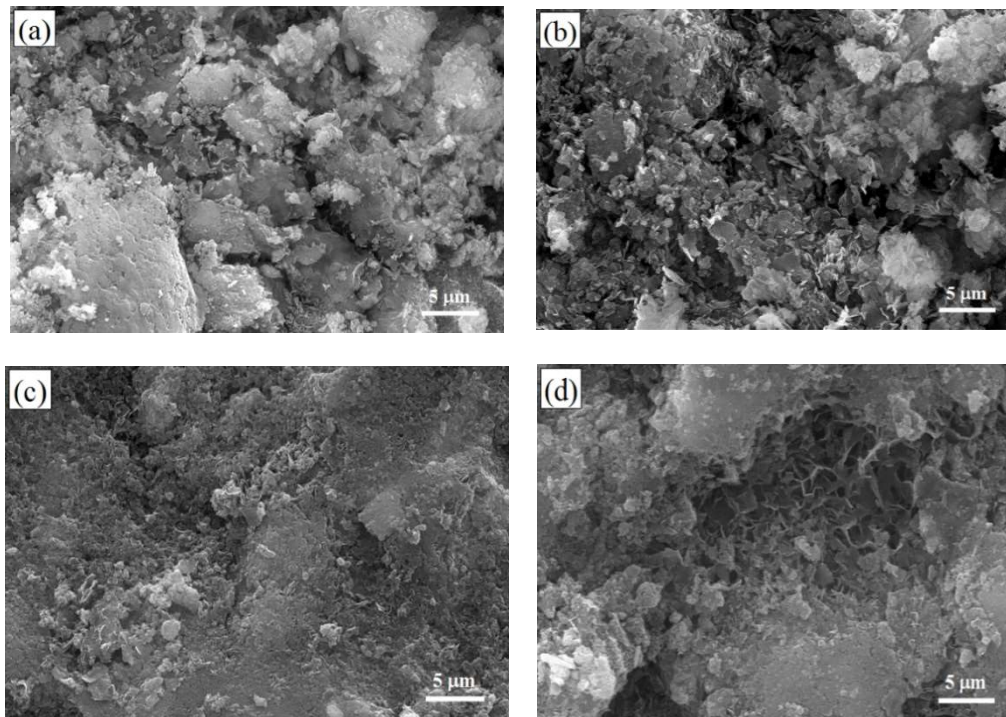


Figure 10. FESEM images of (a) Zn; (b) SiC/Zn; (c) POT-SiC/Zn and (d) PMT-SiC/Zn coatings immersed in 3.5% NaCl solution for 90 days.

According to the presented results, it can be speculated that the role of the outer POT film in total corrosion protection is related to its physical and electronic barrier effects. Under the attacks of corrosion medium, POT is expected to capture the ions released during the corrosion reaction of the inner SiC/Zn surface and get doped and release the dopant ions [46]. It works as a self-healing coating and forms a dense passive layer of ZnO and the insoluble $Zn(C_{18}H_{29}SO_3)_2$ compounds between the POT film and the SiC/Zn coating. The role of the inner SiC/Zn coating in total corrosion protection is related to its barrier effect. The surface and electrochemical corrosion analysis has shown that the addition of SiC nanoparticles into the Zn matrix decreases significantly the effective metallic area for corrosion. When the corrosion medium penetrates the POT film with the increase of immersing time, the ordinary physical combination between the Zn matrix and SiC nanoparticles can be easily translated into the steady chemical combination, forming $Zn_x(SiC)_y$ complex compounds with zinc ions which could increase the barrier effects of inner surface. Furthermore, the electrons generated by the local anodic reaction of the SiC/Zn coating are captured by POT and are transferred to the interface of the POT film/electrolyte, thus avoiding shedding of the POT film and protection failure due to cathodic reaction occurring at the SiC/Zn surface.

4. Conclusions

The poly(o/m-toluidine) films were chemically deposited on the surfaces of SiC/Zn coatings by solution evaporation method. The structures of poly(o/m-toluidine) showed that the positions of methyl have a greater influence on poly-toluidine, and that the ortho-methyl improves the protonated doping level, structural compactness, and electrochemical activity of POT. The surface morphologies of all coatings showed that SiC nanoparticles reduce the pore and groove defects of the zinc matrix, which promotes the inlay bonding between polymer film and composite SiC/Zn coating. The electrochemical corrosion measurements and accelerated immersion test of all coatings revealed that the corrosion resistance of poly(o/m-toluidine)-SiC/Zn bilayer coatings were higher than that of electrodeposited coatings, and that POT-SiC/Zn bilayer coatings were more protective. The excellent corrosion protection capability of POT-SiC/Zn bilayer coatings was attributed to the fact that the stronger adsorptive and continuous POT film ensures that the denser passivation film produces the interface of the POT film and the SiC/Zn surface. Therefore, it is foreseeable that conducting polymers as an effective corrosion inhibitor for composite electrodeposited coatings have potential industrial application prospects in the near future.

Author Contributions: C.H. and Y.L. conceived and designed the experimental scheme, C.H., J.Z. and W.H. performed the experimental work, and C.H. analyzed the results and wrote the manuscript.

Funding: This research was funded by the National Natural Science Foundation of China (51774076, 51474057 and 51704063), the Fundamental Research Funds for the Central Universities (N172507011 and N172506010).

Conflicts of Interest: The authors declare no conflict of interest.

References

1. Sajjadnejad, M.; Mozafari, A.; Omidvar, H.; Javanbakht, M. Preparation and corrosion resistance of pulse electrodeposited Zn and Zn-SiC nanocomposite coatings. *Appl. Surf. Sci.* **2014**, *300*, 1–7. [[CrossRef](#)]
2. Youssef, K.M.S.; Koch, C.C.; Fedkiw, P.S. Improved corrosion behavior of nanocrystalline zinc produced by pulse-current electrodeposition. *Corros. Sci.* **2004**, *46*, 51–64. [[CrossRef](#)]
3. Qing, Y.Q.; Yang, C.N.; Yu, Z.Y.; Zhang, Z.F.; Hu, Q.L.; Liu, C.S. Large-area fabrication of superhydrophobic zinc surface with reversible wettability switching and anticorrosion. *J. Electrochem. Soc.* **2016**, *163*, D385–D391. [[CrossRef](#)]
4. Vlasa, A.; Varvara, S.; Pop, A.; Bulea, C.; Muresan, L.M. Electrodeposited Zn-TiO₂ nanocomposite coatings and their corrosion behavior. *J. Appl. Electrochem.* **2010**, *40*, 1519–1527. [[CrossRef](#)]
5. Nemes, P.I.; Lekka, M.; Fedrizzi, L.; Muresan, L.M. Influence of the electrodeposition current regime on the corrosion resistance of Zn-CeO₂ nanocomposite coatings. *Surf. Coat. Technol.* **2014**, *252*, 102–107. [[CrossRef](#)]
6. Sen, R.; Bhattacharya, S.; Das, S.; Das, K. Effect of surfactant on the co-electrodeposition of the nano-sized ceria particle in the nickel matrix. *J. Alloys Compd.* **2010**, *489*, 650–658. [[CrossRef](#)]
7. Praveen, B.M.; Venkatesha, T.V. Electrodeposition and properties of Zn-nanosized TiO₂ composite coatings. *Appl. Surf. Sci.* **2008**, *254*, 2418–2424. [[CrossRef](#)]
8. Vathsala, K.; Venkatesha, T.V. Zn-ZrO₂ nanocomposite coatings: Electrodeposition and evaluation of corrosion resistance. *Appl. Surf. Sci.* **2011**, *257*, 8929–8936. [[CrossRef](#)]
9. Ryu, H.; Sheng, N.; Ohtsuka, T.; Fujita, S.; Kajiyama, H. Polypyrrole film on 55% Al-Zn-coated steel for corrosion prevention. *Corros. Sci.* **2012**, *56*, 67–77. [[CrossRef](#)]
10. Meng, Y.N.; Wang, K.; Zhang, Y.J.; Wei, Z.X. Hierarchical porous graphene/polyaniline composite film with superior rate performance for flexible supercapacitors. *Adv. Mater.* **2013**, *25*, 6985–6990. [[CrossRef](#)] [[PubMed](#)]
11. Kumar, S.A.; Meenakshi, K.S.; Sankaranarayanan, T.S.N.; Srikanth, S. Corrosion resistant behaviour of PANI-metal bilayer coatings. *Prog. Org. Coat.* **2008**, *62*, 285–292. [[CrossRef](#)]
12. Mostafaei, A.; Nasirpouri, F. Epoxy/polyaniline-ZnO nanorods hybrid nanocomposite coatings: Synthesis, characterization and corrosion protection performance of conducting paints. *Prog. Org. Coat.* **2014**, *77*, 146–159. [[CrossRef](#)]
13. Lehr, I.L.; Saidman, S.B. Anticorrosive properties of polypyrrole films modified with zinc onto SAE 4140 steel. *Prog. Org. Coat.* **2013**, *76*, 1586–1593. [[CrossRef](#)]

14. Sheng, N.; Lei, Y.H.; Hyonoo, A.; Ueda, M.; Ohtsuka, T. Improvement of polypyrrole films for corrosion protection of zinc-coated AZ91D alloy. *Prog. Org. Coat.* **2014**, *77*, 1724–1734. [[CrossRef](#)]
15. Tüken, T.; Yazıcı, B.; Erbil, M. Zinc modified polyaniline coating for mild steel protection. *Mater. Chem. Phys.* **2006**, *99*, 459–464. [[CrossRef](#)]
16. Li, Z.T.; Ma, L.; Li, W.L.; Gan, M.Y.; Qiu, W.; Yan, J. Characterization and anticorrosive properties of poly(2,3-dimethylaniline)/nano- Al_2O_3 composite synthesized by emulsion polymerization. *Polym. Adv. Technol.* **2013**, *24*, 847–852. [[CrossRef](#)]
17. Bilal, S.; Farooq, S.; Shah, A.A.; Holze, R. Improved solubility, conductivity, thermal stability and corrosion protection properties of poly(o-toluidine) synthesized via chemical polymerization. *Synth. Met.* **2014**, *197*, 144–153. [[CrossRef](#)]
18. Hu, C.B.; Li, Y.; Kong, Y.Z.; Ding, Y.S. Preparation of poly(o-toluidine)/nano ZnO/epoxy composite coating and evaluation of its corrosion resistance properties. *Synth. Met.* **2016**, *214*, 62–70. [[CrossRef](#)]
19. Wang, Y.Y.; Normand, B.; Suo, X.K.; Planche, M.; Liao, H.; Tang, J.L. Cold-sprayed AZ91D coating and SiC/AZ91D composite coatings. *Coatings* **2018**, *8*, 122. [[CrossRef](#)]
20. Hu, C.B.; Li, Y.; Zhang, N.; Zhang, J.W. Preparation of poly(o-ethylaniline)-SiC/zinc bilayer coatings and study of its corrosion resistance properties. *J. Electrochem. Soc.* **2018**, *165*, G56–G65. [[CrossRef](#)]
21. Hesampour, M.; Taher, M.A.; Behzadi, M. Synthesis, characterization and application of a MnFe_2O_4 @poly(o-toluidine) nanocomposite for magnetic solid-phase extraction of polycyclic aromatic hydrocarbons. *New J. Chem.* **2017**, *41*, 12910–12919. [[CrossRef](#)]
22. Hwang, J.J.; Soto, C.; Lafaurie, D.; Stephen, M.; Sarno, D.M. Porous microspheres of polyaniline, poly(o-toluidine), and poly(m-toluidine) prepared from double emulsions stabilized by toluidine isomers as the single surfactant. *J. Colloid Interface Sci.* **2018**, *513*, 331–341. [[CrossRef](#)] [[PubMed](#)]
23. Ashokan, S.; Ponnuswamy, V.; Jayamurugan, P.; Chandrasekaran, J.; Rao, Y.V.S. Influence of the counter ion on the properties of organic and inorganic acid doped polyaniline and their schottky diodes. *Superlattices Microstruct.* **2015**, *85*, 282–293. [[CrossRef](#)]
24. Song, M.K.; Kim, Y.T.; Kim, B.S.; Kim, J.; Char, K.; Rhee, H.W. Synthesis and characterization of soluble polypyrrole doped with alkylbenzenesulfonic acids. *Synth. Met.* **2004**, *141*, 315–319. [[CrossRef](#)]
25. Niu, M.J.; Kong, X.J. Efficient biodiesel production from waste cooking oil using p-toluenesulfonic acid doped polyaniline as a catalyst. *RSC Adv.* **2015**, *5*, 27273–27277. [[CrossRef](#)]
26. Golczak, S.; Kanciurzevska, A.; Fahlman, M.; Langer, K.; Langer, J.J. Comparative XPS surface study of polyaniline thin films. *Solid State Ion.* **2008**, *179*, 2234–2239. [[CrossRef](#)]
27. Saini, P.; Arora, M.; Gupta, G.; Gupta, B.K.; Singh, V.N.; Choudhary, V. High permittivity polyaniline–barium titanate nanocomposites with excellent electromagnetic interference shielding response. *Nanoscale* **2013**, *5*, 4330–4336. [[CrossRef](#)] [[PubMed](#)]
28. Shinde, V.P.; Patil, P.P. Investigation on role of monomer(s) during electrochemical polymerization of aniline and its derivatives on low carbon steel by XPS. *Electrochim. Acta* **2012**, *78*, 483–494. [[CrossRef](#)]
29. Wang, Y.G.; Li, H.Q.; Xia, Y.Y. Ordered whiskerlike polyaniline grown on the surface of mesoporous carbon and its electrochemical capacitance performance. *Adv. Mater.* **2006**, *18*, 2619–2623. [[CrossRef](#)]
30. Cong, H.P.; Ren, X.C.; Wang, P.; Yu, S.H. Flexible graphene–polyaniline composite paper for high-performance supercapacitor. *Energy Environ. Sci.* **2013**, *6*, 1185–1191. [[CrossRef](#)]
31. Bavastrello, V.; Carrara, S.; Ram, M.K.; Nicolini, C. Optical and electrochemical properties of poly(o-toluidine) multiwalled carbon nanotubes composite langmuir-schaefer films. *Langmuir* **2004**, *20*, 969–973. [[CrossRef](#)] [[PubMed](#)]
32. Bilal, S.; Holze, R. Electrochemical copolymerization of m-toluidine and o-phenylenediamine. *Electrochim. Acta* **2006**, *52*, 1247–1257. [[CrossRef](#)]
33. Xia, X.L.; Zhitomirsky, I.; McDermid, J.R. Electrodeposition of zinc and composite zinc-yttria stabilized zirconia coatings. *J. Mater. Process. Technol.* **2009**, *209*, 2632–2640. [[CrossRef](#)]
34. Azizi, M.; Schneider, W.; Plieth, W. Electrolytic co-deposition of silicate and mica particles with zinc. *J. Solid State Electrochem.* **2005**, *9*, 429–437. [[CrossRef](#)]
35. Yuan, X.T.; Wang, Y.; Sun, D.B.; Yu, H.Y. Influence of pulse parameters on the microstructure and microhardness of nickel electrodeposits. *Surf. Coat. Technol.* **2008**, *202*, 1895–1903.

36. Benchikh, A.; Aitout, R.; Makhloufi, L.; Benhaddad, L.; Saidani, B. Soluble conducting poly(aniline-co-orthotoluidine) copolymer as corrosion inhibitor for carbon steel in 3% NaCl solution. *Desalination* **2009**, *249*, 466–474. [[CrossRef](#)]
37. Sajjadnejad, M.; Ghorbani, M.; Afshar, A. Microstructure-corrosion resistance relationship of direct and pulse current electrodeposited Zn–TiO₂ nanocomposite coatings. *Ceram. Int.* **2015**, *41*, 217–224. [[CrossRef](#)]
38. Ortiz, Z.I.; Díaz-Arista, P.; Meas, Y.; Ortega-Borges, R.; Trejo, G. Characterization of the corrosion products of electrodeposited Zn, Zn–Co and Zn–Mn alloys coatings. *Corros. Sci.* **2009**, *51*, 2703–2715. [[CrossRef](#)]
39. Farzaneh, A.; Mohammadi, M.; Ehteshamzadeh, M.; Monhamedi, F. Electrochemical and structural properties of electroless Ni–P–SiC nanocomposite coatings. *Appl. Surf. Sci.* **2013**, *276*, 697–704. [[CrossRef](#)]
40. Xing, C.J.; Zhang, Z.M.; Yu, L.M.; Waterhouse, G.I.N.; Zhang, L.J. Anti-corrosion performance of nanostructured poly(aniline-co-metanilic acid) on carbon steel. *Prog. Org. Coat.* **2014**, *77*, 354–360. [[CrossRef](#)]
41. Sathiyarayanan, S.; Balakrishnan, K.; Dhawan, S.K.; Trivedi, D.C. Prevention of corrosion of iron in acidic media using poly(o-methoxy-aniline). *Electrochim. Acta* **1994**, *39*, 831–837. [[CrossRef](#)]
42. Chaudhari, S.; Sainkar, S.R.; Patil, P.P. Poly(o-ethylaniline) coatings for stainless steel protection. *Prog. Org. Coat.* **2007**, *58*, 54–63. [[CrossRef](#)]
43. Chaudhari, S.; Sainkar, S.R.; Patil, P.P. Anticorrosive properties of electrosynthesized poly(o-anisidine) coatings on copper from aqueous salicylate medium. *J. Phys. D Appl. Phys.* **2007**, *40*, 520–533. [[CrossRef](#)]
44. Deyab, M.A. Corrosion protection of aluminum bipolar plates with polyaniline coating containing carbon nanotubes in acidic medium inside the polymer electrolyte membrane fuel cell. *J. Power Sources* **2014**, *268*, 50–55. [[CrossRef](#)]
45. Chaudhari, S.; Patil, P.P. Inhibition of nickel coated mild steel corrosion by electrosynthesized polyaniline coatings. *Electrochim. Acta* **2011**, *56*, 3049–3059. [[CrossRef](#)]
46. Li, Z.T.; Ma, L.; Gan, M.Y.; Qiu, W.; Fu, D.D.; Li, S.; Bai, Y.Q. Synthesis and anticorrosion performance of poly(2,3-dimethylaniline)–TiO₂ composite. *Prog. Org. Coat.* **2013**, *76*, 1161–1167. [[CrossRef](#)]



© 2018 by the authors. Licensee MDPI, Basel, Switzerland. This article is an open access article distributed under the terms and conditions of the Creative Commons Attribution (CC BY) license (<http://creativecommons.org/licenses/by/4.0/>).